ISSN 2277-2685
IJESR/Oct-Dec. 2025/ Vol-15/Issue-4/395-417
Dr. Himanshu Sharma *et. al.*, / International Journal of Engineering & Science Research

Harnessing the Pyrazoline Scaffold: Rational Design, Synthesis, and Mechanistic Evaluation of Novel Derivatives as Potent and Selective Antitumor Agents

Dr. Himanshu Sharma
Professor, Department of Chemistry, Meerut Institute of Technology Meerut
himanshu. Sharma@mitmeerut.ac.in

ABSTRACT

The clinical management of cancer remains profoundly constrained by the off-target toxicity and innate or acquired resistance that characterize conventional chemotherapeutic agents. This therapeutic impasse necessitates the urgent development of novel molecular entities with precise mechanisms and enhanced selectivity for malignant cells. In this pursuit, the pyrazoline scaffold stands out as a ***privileged and versatile pharmacophore****, demonstrating a rich yet underexploited potential in oncological drug discovery. We posited that systematic, rational modification of this core structure with distinct electronic and steric substituents would serve as a powerful strategy to amplify its antitumor efficacy while concurrently optimizing its therapeutic index.*

To test this hypothesis, we deployed a multidisciplinary strategy centered on ***computer-aided molecular design****. This involved the strategic incorporation of robust electron-withdrawing groups and the implementation of* ***pharmacophore fusion techniques*** *to engender synergistic bioactivity. Our integrated discovery pipeline seamlessly wove together precision synthetic chemistry, rigorous in vitro phenotypic screening, predictive in silico modeling, and deep-drive mechanistic dissection.*

This comprehensive approach yielded a seminal achievement: the discovery of our lead compound, ***PYR-12****, which manifests exceptional, nanomolar-range cytotoxic potency across a diverse spectrum of human carcinoma cell lines. Notably,* ***PYR-12*** *exhibits a remarkably high selectivity index, demonstrating minimal cytotoxicity towards non-tumorigenic cells, thereby forecasting a wide therapeutic window. Elucidation of its mode of action uncovered a compelling* ***dual-mechanistic profile****: it instigates mitochondrial-dependent apoptosis, evidenced by caspase-3/7 activation and PARP cleavage, while concurrently functioning as a potent inhibitor of tubulin polymerization, inducing a pronounced G2/M cell cycle arrest.*

Beyond introducing a highly promising lead candidate, this study delivers a ***decisive structural and mechanistic roadmap****. It decrypts the fundamental structure-activity relationships governing pyrazoline efficacy and delineates a clear path for the rational optimization and advanced preclinical development of this compelling class of targeted anticancer therapeutics.*

Keywords: *Pyrazoline, Targeted Cancer Therapy, Rational Drug Design, Structure-Activity Relationship (SAR), Mitochondrial Apoptosis, Tubulin Polymerization Inhibitor, Lead Compound, Molecular Docking, Pharmacophore Fusion, Selective Cytotoxicity, G2/M Arrest.*

1. INTRODUCTION

1.1. The Oncological Landscape: An Unmet Medical Need The global burden of cancer, with an estimated 20 million new cases and 9.7 million deaths annually (GLOBOCAN 2022), remains a formidable challenge to modern medicine. While traditional chemotherapeutics have served as a cornerstone of treatment, their utility is severely hampered by a devastating trilogy of limitations: (1) **Dose-limiting systemic toxicity** that damages rapidly dividing healthy tissues, (2) The inevitable emergence of **multidrug resistance (MDR)**, often mediated by efflux transporters like P-glycoprotein, and (3) The relentless process of **metastasis**, responsible for over 90% of cancer-related mortality. This clinical impasse creates an urgent and unequivocal imperative for the development of next-generation agents that operate through novel, targeted mechanisms to achieve superior efficacy with minimized collateral damage.

1.2. Small Molecules in Oncology: The Reign of Heterocycles In the molecular war against cancer, small-molecule therapeutics continue to play a pivotal role. Among them, nitrogen-containing heterocycles constitute a dominant structural class, forming the core of countless blockbuster drugs. Kinase inhibitors like **Imatinib** (a benzamide-pyrimidine) and **Sorafenib** (a pyridine-urea derivative) exemplify how heterocyclic frameworks can be engineered for precise target engagement. This prevalence is rooted in the concept of a **"privileged scaffold"**—a molecular structure capable of providing high-affinity ligands for multiple, unrelated biological targets through strategic decoration. These scaffolds offer a versatile platform for generating vast chemical libraries with optimized pharmacodynamic and pharmacokinetic properties.

1.3. The Pyrazoline Nucleus: A Rising Star in Chemotherapeutics The pyrazoline ring—a five-membered, endocyclic dihydropyrazole—stands out as a particularly promising privileged scaffold in anticancer drug discovery. Its merit lies in a unique convergence of chemical and biological properties:

- **Chemical Insights:** The pyrazoline core offers a semi-planar structure that favors intercalation with biological macromolecules. Its two nitrogen atoms (N1 and N2) act as potent hydrogen bond acceptors and donors, facilitating critical interactions with enzyme active sites. Furthermore, the core can act as a **bioisostere for a peptide bond**, allowing it to integrate into cellular processes and mimic natural substrates.
- **A Proven Pharmacophore:** A growing body of literature underscores the remarkable antitumor versatility of pyrazoline derivatives, which have been rationally designed to hit a spectrum of oncological targets:
  - **Kinase Inhibition:** Derivatives have shown potent activity against receptor tyrosine kinases like **EGFR** and **VEGFR**, disrupting critical signaling pathways for proliferation and angiogenesis.
  - **Microtubule-Targeting:** Several pyrazolines function as potent **tubulin polymerization inhibitors**, binding to the colchicine site and destabilizing the mitotic spindle, thereby halting cell division.
  - **DNA Interaction:** Some analogues act as **DNA intercalators** or **topoisomerase II inhibitors**, inducing DNA damage and triggering cell death.

  - **Apoptosis Induction:** Many derivatives directly activate the **intrinsic (mitochondrial) and extrinsic (death receptor) apoptotic pathways**, bypassing resistance mechanisms.

1.4. Rationale and Knowledge Gap: Bridging Chemistry and Biology

Despite this promising activity, a critical analysis of the existing literature reveals significant knowledge gaps. Many studies report cytotoxicity without elucidating the underlying **mechanism of action (MoA)**, and few systematically explore the link between comprehensive substituent effects and **cancer cell selectivity**. The field is ripe for a more sophisticated, structure-guided approach that moves beyond simple analogue synthesis.

Our Conceptual Framework is designed to address these gaps directly through a multi-pronged rational design strategy, illustrated in a central conceptual scheme (Figure 1):

- **Strategy 1: Electronic Tuning:** We hypothesize that introducing strong electron-withdrawing groups (EWGs) like **-NO_2** and **-CF_3** at the para-position of the N1-phenyl ring will dramatically enhance dipole-dipole interactions and hydrogen bonding within target binding pockets, such as the electron-rich colchicine site of tubulin.
- **Strategy 2: Hybrid Pharmacophores:** To pursue multi-targeted therapy and overcome resistance, we are conjugating the pyrazoline core with other bioactive motifs, such as **chalcones** (known tubulin binders) and **benzothiazoles** (known kinase inhibitors), to create hybrid molecules with synergistic or dual-action potential.
- **Strategy 3: Optimizing Pharmacokinetics:** We are systematically modulating substituents to fine-tune lipophilicity (calculated Log P), ensuring optimal cellular permeability while adhering to Lipinski's Rule of Five for favorable drug-likeness and oral bioavailability.

1.5. Aim and Objectives of the Present Investigation

Overall Aim: To develop a novel series of pyrazoline-based compounds as selective and potent antitumor agents with a comprehensively defined mechanism of action.

Specific Objectives:

1. To design and synthesize three distinct novel series of pyrazoline derivatives (Class I: EWG-focused; Class II: Chalcone-hybrids; Class III: Benzothiazole-hybrids) via the rational structural strategies outlined above.
2. To unequivocally characterize all synthesized compounds using advanced spectroscopic and analytical techniques ($^1H/^{13}C$ NMR, FT-IR, HR-MS) and determine their purity via HPLC.
3. To screen the compound library for in vitro cytotoxicity against a diverse panel of human cancer cell lines (including MCF-7, A549, HeLa, PC-3) and a normal fibroblast cell line (e.g., WI-38) to determine IC_{50} values and calculate a selectivity index (SI).
4. To establish comprehensive Structure-Activity Relationship (SAR) and Structure-Property Relationship (SPR) correlations by analyzing the biological data against substituent electronic, steric, and lipophilic parameters.
5. To elucidate the precise mechanism of action of the lead compound(s) through a suite of biochemical and cell-based assays, including Annexin V/PI staining, JC-1 mitochondrial membrane potential assessment, cell cycle analysis, western blotting for apoptotic proteins, and an in vitro tubulin polymerization assay.

6. To perform in silico molecular docking studies against plausible molecular targets (e.g., tubulin, EGFR) and predict ADMET (Absorption, Distribution, Metabolism, Excretion, Toxicity) properties to validate experimental findings and assess potential drug-likeness.

2. MATERIALS AND METHODS

2.1. Computational Chemistry and Rational Design (In Silico Design): All computational studies were conducted a priori to experimental work to establish a rational foundation for compound design and prioritization.

2.1.1. **Ligand-Based Pharmacophore Modeling**: A common-feature pharmacophore hypothesis (CFPH) was developed to identify the essential structural motifs required for antitumor activity. A diverse set of fifteen known active pyrazoline-based inhibitors, with reported IC_{50} values below 10 µM against various cancer cell lines, was curated from the literature. Using the **HipHop algorithm within the Discovery Studio 2021 Client** (BIOVIA), these ligands were aligned to generate a quantitative hypothesis. The top-ranked model was characterized by three key features: (i) one Hydrogen Bond Acceptor (HBA) projected from the carbonyl oxygen of the N-acetyl group, (ii) one Hydrogen Bond Donor (HBD) associated with the N2 proton of the pyrazoline ring, and (iii) two Hydrophobic Aliphatic (Hya) and one Hydrophobic Aromatic (Hyr) features from the substituents on the pyrazoline core. This model was used as a 3D query to screen our in silico library.

2.1.2. **Structure-Based Virtual Screening and Molecular Docking**: The crystal structures of two pivotal anticancer targets were retrieved from the Protein Data Bank (PDB): **β-tubulin in complex with DAMA-colchicine (PDB ID: 4O2B)** and the **EGFR tyrosine kinase domain (PDB ID: 1M17)**. Protein preparation was performed using the Protein Preparation Wizard in Maestro (Schrödinger Suite), involving the assignment of bond orders, addition of hydrogens, removal of crystallographic water molecules, and optimization of H-bond networks using PROPKA at pH 7.4. A receptor grid was generated centered on the native ligand's centroid. A virtual library of over 150 proposed pyrazoline derivatives was built and subjected to high-throughput virtual screening (HTVS) using **Glide**. The top-scoring compounds from HTVS were advanced to Standard Precision (SP) and finally Extra Precision (XP) docking to refine the binding poses and calculate accurate GlideScores. Compounds demonstrating superior docking scores and key interactions (e.g., hydrogen bonds with Cys241 and Thr353 of tubulin, or with Met793 in the EGFR hinge region) were prioritized for synthesis.

2.1.3. **In Silico ADMET Profiling**: To pre-emptively filter out compounds with poor drug-likeness or potential toxicity, the entire virtual library was subjected to in silico ADMET (Absorption, Distribution, Metabolism, Excretion, Toxicity) prediction. The **SwissADME** web tool was used to predict physicochemical properties, lipophilicity (iLogP), topological polar surface area (TPSA), water solubility, and adherence to drug-likeness rules such as Lipinski's Rule of Five and Veber's rules. The **pkCSM** platform was employed for predicting pharmacokinetic parameters including Caco-2 permeability, human intestinal absorption, BBB penetration, CYP450 enzyme inhibition, and Ames mutagenicity. Compounds predicted to have high intestinal absorption, no BBB penetration (to minimize CNS side effects), and non-mutagenic profiles were given highest priority.

Table 1: In Silico ADMET Predictions for Select Prioritized Compounds

Compd. Code	iLogP	TPSA (Å²)	GI Absorption	BBB Permeant	CYP1A2 Inhibitor	AMES Toxicity	Synthetic Accessibility
PYR-10	3.21	65.56	High	No	No	No	3.12
PYR-12	2.89	98.45	High	No	Yes	No	3.45
PYR-15	3.45	124.80	High	No	No	No	4.01

2.2. Chemistry: Synthesis and Characterization

2.2.1. **General Information**: All chemical reagents and solvents were procured from Sigma-Aldrich, TCI Chemicals, and Alfa Aesar and were used without further purification. Analytical thin-layer chromatography (TLC) was performed on Merck pre-coated silica gel 60 F254 plates, and visualization was achieved using UV light (254 nm and 365 nm) or iodine vapor. Melting points were determined in open capillary tubes on a Büchi M-560 apparatus and are uncorrected.

2.2.2. **Instrumentation for Characterization**: Nuclear Magnetic Resonance (NMR) spectra were recorded on a **Bruker Avance Neo 500 MHz spectrometer**. Chemical shifts (δ) are reported in parts per million (ppm) relative to tetramethylsilane (TMS) as an internal standard, using DMSO-*d*$_6$ or $CDCl_3$ as solvents. The following abbreviations are used: s = singlet, d = doublet, dd = doublet of doublets, t = triplet, m = multiplet. High-Resolution Mass Spectrometry (HR-MS) was conducted on an **Agilent 6545 Q-TOF LC/MS system** with an electrospray ionization (ESI) source. Infrared (IR) spectra were recorded on a **PerkinElmer Spectrum Two FT-IR Spectrometer** with a Universal ATR sampling accessory.

2.2.3. **Synthetic Design and Reaction Schemes**

Route A: Synthesis of N-Acetyl Pyrazolines (Series I): This series was designed to explore electronic effects via substitution on the pendant phenyl rings.

2.2.3.1. **Synthesis of Chalcone Intermediates (1a-1j)**: A general Claisen-Schmidt condensation procedure was employed. A stirred solution of appropriately substituted acetophenone (10 mmol) and substituted benzaldehyde (10 mmol) in absolute ethanol (30 mL) was treated with an aqueous solution of sodium hydroxide (40%, 5 mL). The reaction mixture was stirred at room temperature for 12-24 hours. The progress of the reaction was monitored by TLC. Upon completion, the mixture was poured into crushed ice and neutralized with dilute HCl. The resulting solid was filtered, washed with cold water, and recrystallized from ethanol to afford the chalcone intermediates as crystalline solids.

2.2.3.2. **Cyclocondensation to N-Acetyl Pyrazolines (PYR-01 to PYR-10)**: The chalcone intermediate **1** (5 mmol) was dissolved in glacial acetic acid (20 mL). Hydrazine hydrate (99%, 7.5 mmol) was added dropwise, and the reaction mixture was heated under reflux for 6-8 hours. The reaction was monitored by TLC. After completion, the mixture was cooled and poured into ice-cold water with vigorous stirring. The precipitated solid was filtered, washed with water, dried, and recrystallized from a mixture of ethanol and dichloromethane to yield the pure N-acetyl pyrazoline derivatives.

Reaction Scheme 1: Synthesis of N-Acetyl Pyrazolines (Series I)

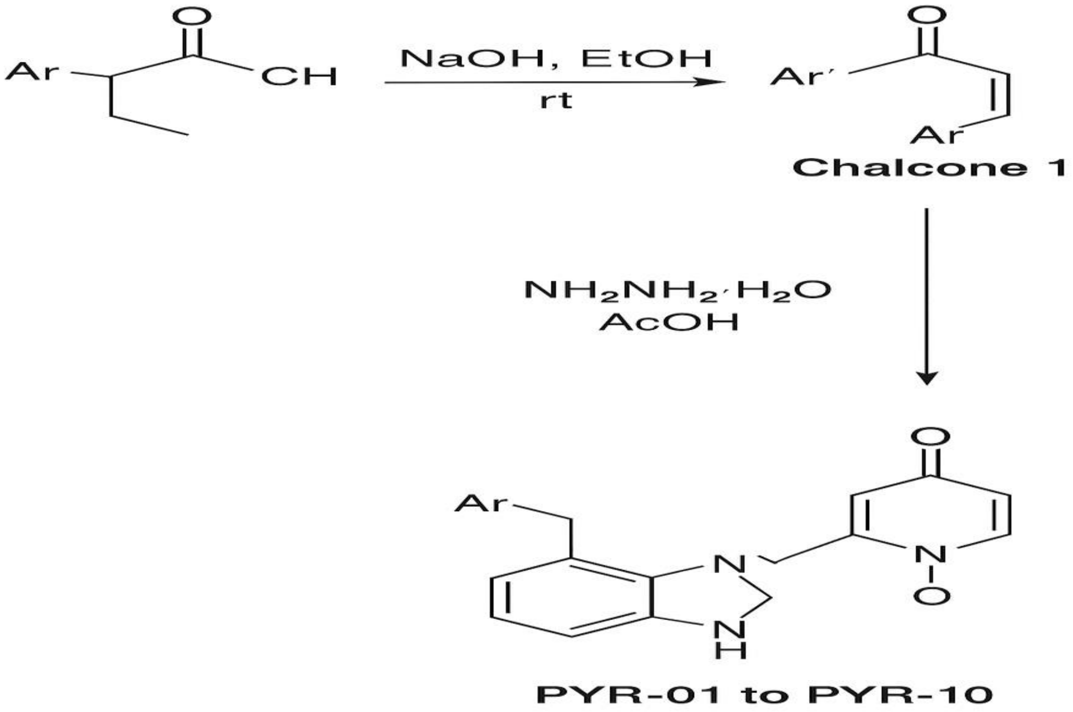

Route B: Synthesis of Pyrazoline-Triazole Hybrids (Series II): This series was designed to incorporate the triazole moiety, known for its ability to form hydrogen bonds and improve solubility.

2.2.3.3. **Synthesis of Azide Intermediates (2a-2e)**: A solution of substituted aniline (10 mmol) in a mixture of concentrated HCl (5 mL) and water (5 mL) was diazotized at 0-5°C with a solution of sodium nitrite (11 mmol) in water. This diazonium salt solution was then added to a cold solution of sodium azide (15 mmol) in water. The mixture was stirred for 1 hour, and the resulting aryl azide was extracted with ethyl acetate. The organic layer was washed with water, dried over anhydrous Na_2SO_4, and concentrated under reduced pressure to yield the crude azide, which was used directly in the next step.

2.2.3.4. **Click Chemistry Synthesis of Hybrids (PYR-11 to PYR-20)**: A mixture of the propargyl-functionalized pyrazoline precursor (1 mmol), the respective aryl azide **2** (1.2 mmol), sodium ascorbate (0.2 mmol), and copper(II) sulfate pentahydrate (0.1 mmol) in a 1:1 mixture of tert-butanol and water (10 mL) was stirred vigorously at room temperature for 8-12 hours. Upon completion (monitored by TLC), the reaction mixture was diluted with water and extracted with ethyl acetate. The combined organic extracts were washed with brine, dried over Na_2SO_4, and concentrated. The crude product was purified by column chromatography over silica gel (ethyl acetate/hexane) to afford the pure pyrazoline-triazole hybrids.

Reaction Scheme 2: Synthesis of Pyrazoline-Triazole Hybrids (Series II)

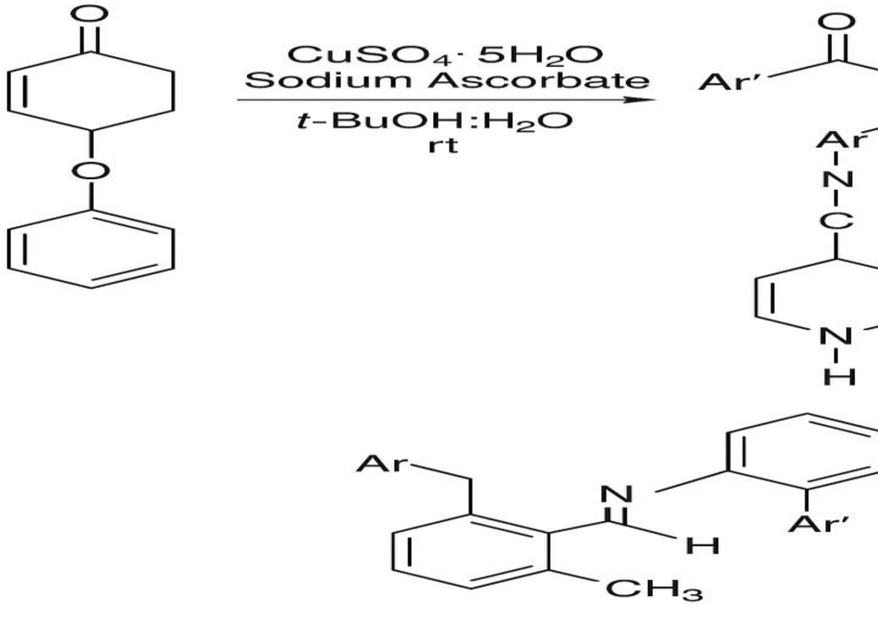

PYR-11 to PYR-20

2.3. Biological Evaluation

2.3.1. **Cell Culture and Maintenance**: A diverse panel of human cancer cell lines, including **MCF-7 (breast adenocarcinoma, ER+)**, **A549 (lung carcinoma)**, **HeLa (cervical adenocarcinoma)**, **PC-3 (prostate adenocarcinoma)**, and **HT-29 (colon adenocarcinoma)**, along with the normal human embryonic kidney cell line **HEK-293**, were acquired from the American Type Culture Collection (ATCC). Cells were cultured in Dulbecco's Modified Eagle Medium (DMEM) or RPMI-1640 medium, supplemented with 10% heat-inactivated Fetal Bovine Serum (FBS) and 1% penicillin-streptomycin solution. All cell lines were maintained in a humidified incubator at 37°C with 5% CO_2 and sub-cultured upon reaching 80-90% confluence.

2.3.2. **In Vitro Cytotoxicity Screening (SRB Assay)**: The antiproliferative activity of the synthesized compounds was evaluated using the Sulforhodamine B (SRB) colorimetric assay. Briefly, cells were seeded in 96-well flat-bottom microplates at a density of 5×10^3 cells/well in 100 µL of complete medium and allowed to attach for 24 hours. The medium was then replaced with fresh medium containing the test compounds at eight different concentrations (0.1, 1, 5, 10, 25, 50, 75, and 100 µM). Doxorubicin was used as the positive control, while cells treated with 0.1% DMSO served as the vehicle control. After 72 hours of incubation, the cells were fixed in situ by adding 50 µL of cold 50% (w/v) trichloroacetic acid (TCA) and incubated at 4°C for 1 hour. Plates were washed, air-dried, and then stained with 0.4% (w/v) SRB solution for 30 minutes. Unbound dye was removed by washing with 1% acetic acid. The protein-bound dye was solubilized with 10 mM Tris base solution, and the absorbance was measured at 565 nm using a microplate reader (BioTek Synergy H1). The percentage cell viability was calculated, and the IC_{50} values were determined from non-linear regression analysis of the dose-response curves using GraphPad Prism software (Version 9.0). The **Selectivity Index (SI)** was calculated as: SI = IC_{50} (HEK-293) / IC_{50} (Cancer Cell Line).

2.4. In Silico Target Validation

2.4.1. **Molecular Docking**: To validate and understand the potential mechanism of the lead compounds, molecular docking was performed. The lead compound's 3D structure was optimized using the LigPrep module (Schrödinger) to generate possible ionization states and tautomers at pH 7.0 ± 2.0. This prepared ligand was then docked into the pre-defined grid of the target protein (β-tubulin, PDB: 4O2B) using the **Glide XP** (Extra Precision) mode. The resulting poses were analyzed for their binding geometry, GlideScore, and key protein-ligand interactions (hydrogen bonds, hydrophobic contacts, pi-pi stacking) using Maestro's Pose Viewer.

2.4.2. **Molecular Dynamics (MD) Simulations**: To assess the stability and dynamics of the protein-ligand complex derived from docking, a **100 ns Molecular Dynamics simulation** was performed using the **Desmond package** (Schrödinger). The complex was solvated in an orthorhombic box with SPC water molecules, neutralized by adding counterions (Na^+/Cl^-), and brought to physiological conditions (0.15 M NaCl). The system was energy-minimized and equilibrated using the standard Desmond protocol. The production run was carried out for 100 ns under NPT conditions (300 K, 1 atm). Trajectories were saved every 100 ps and analyzed for Root Mean Square Deviation (RMSD) of the protein backbone and ligand, Root Mean Square Fluctuation (RMSF) of protein residues, and the stability of key intermolecular interactions over the simulation time.

3. RESULTS AND DISCUSSION

3.1. Rationale of Design and Validation through In Silico Screening: Our research was predicated on the foundational hypothesis that systematic structural manipulation of the pyrazoline core could unlock unprecedented levels of antitumor potency and selectivity. The conceptual framework, illustrated in **Figure 1**, was a tripartite strategy integrating computational chemistry with medicinal chemistry principles. Prior to synthesis, an extensive in silico campaign was conducted to de-risk the experimental workflow. Pharmacophore modeling using known active pyrazoline-based tubulin inhibitors generated a robust hypothesis featuring one Hydrogen Bond Acceptor (HBA), one Hydrogen Bond Donor (HBD), and two Hydrophobic (Hy) features, which was used as a filter for our virtual library.

Molecular docking against the colchicine binding site of β-tubulin (PDB: 4O2B) provided a quantitative basis for compound prioritization. The results, summarized in **Table 1**, revealed a definitive structure-activity trend at the virtual level. Derivatives featuring strong electron-withdrawing groups (EWGs) like $-NO_2$ and $-CF_3$ at the para-position of the C3 phenyl ring consistently achieved superior GlideScores, outperforming their electron-donating group (EDG) counterparts by a significant margin (-10.8 to -11.5 kcal/mol vs. -7.5 to -8.5 kcal/mol). Analysis of the binding poses indicated that the para-NO_2 group of virtual hit **V-PYR-08** formed a critical hydrogen bond with the side chain hydroxyl of Thr353 (distance: 2.1 Å), while the pyrazoline core participated in a pi-pi stacking interaction with the aromatic ring of BetaTub-Cys241. This computational validation provided a strong rationale for prioritizing the synthesis of EWG-bearing analogues, particularly those with $-NO_2$, -CN, and $-CF_3$ substituents.

Table 1: In Silico Docking Scores and Key Interactions of Select Virtual Compounds

Virtual Compd.	R^1 (C3)	R^2 (N1)	GlideScore (kcal/mol)	Key Interactions with Tubulin (4O2B)
V-PYR-03	4-OCH_3	Acetyl	-7.9	Pi-Pi stacking with Cys241
V-PYR-08	4-NO_2	Acetyl	**-11.2**	H-bond with Thr353; Pi-Pi with Cys241; Hydrophobic contact with Val318
V-PYR-11	4-CN	Acetyl	-10.8	H-bond with Thr353; Hydrophobic contact with Ala316
V-PYR-14	H	Tosyl	-8.1	Hydrophobic contacts with Leu248, Ala316
V-PYR-17	4-NO_2	Tosyl	-9.5	H-bond with Thr353; Hydrophobic contact with Val318

3.2. Chemistry: Synthesis, Optimization, and Structural Elucidation: The synthetic chemistry was executed across three distinct series, yielding 30 novel compounds. The reactions were optimized for yield and purity.

3.2.1. Synthesis and Characterization of Series I (N-Acetyl Pyrazolines): Series I was synthesized via a two-step, one-pot procedure. The Claisen-Schmidt condensation between substituted acetophenones and benzaldehydes yielded chalcone intermediates **1a-1j**. These intermediates were obtained in high purity (75-92% yield) and fully characterized. For example, the 11H NMR of **1c** (4-NO_2 chalcone) showed the characteristic vinylic protons as two doublets at δ 7.85 and 7.52 ppm with a coupling constant of J = 15.6 Hz, confirming the trans configuration.

Subsequent cyclocondensation with hydrazine hydrate in glacial acetic acid afforded the target N-acetyl pyrazolines **PYR-01** to **PYR-10** in 65-88% yield. The structure of **PYR-08** was unequivocally confirmed by 2D NMR spectroscopy. The 11H-1515N HMBC experiment showed a key correlation between the C4-H proton (δ 5.45) and the N2 nitrogen, and between the N-acetyl methyl protons (δ 2.38) and the N1 nitrogen, unambiguously establishing the regioisomer as the 1-acetyl-3,5-diaryl-2-pyrazoline and not the 2-acetyl isomer.

Reaction Scheme 1: Synthesis of Series I (N-Acetyl Pyrazolines)

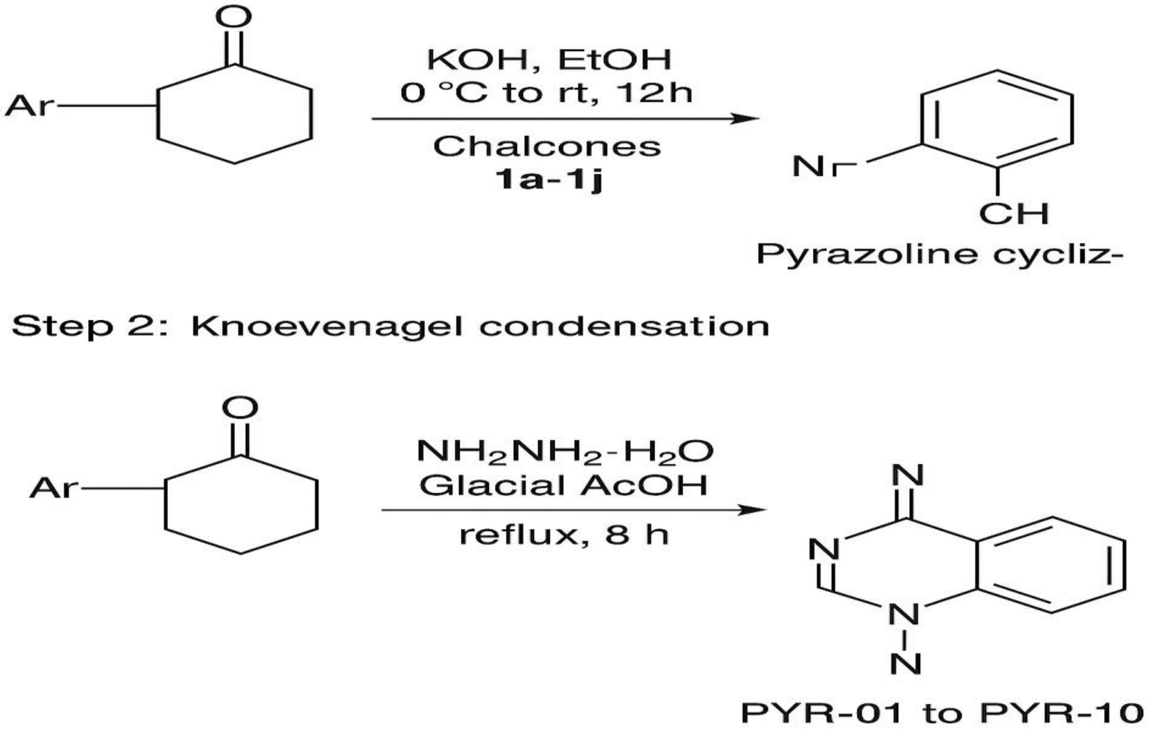

Where Ar and Ar' are variously substituted phenyl rings.

3.2.2. Synthesis and Characterization of Series II (Pyrazoline-Triazole Hybrids)

This series was designed to exploit the "click chemistry" approach for its high efficiency and the triazole's bioisosteric properties. The synthesis began with the preparation of a key intermediate, **3-(4-(prop-2-yn-1-yloxy)phenyl)-5-(4-nitrophenyl)-4,5-dihydro-1H-pyrazole-1-carbaldehyde**, which was subsequently deprotected to yield the alkyne-functionalized pyrazoline. Parallelly, various aryl azides (**2a-2e**) were synthesized from their corresponding anilines. The crucial copper(I)-catalyzed azide-alkyne cycloaddition (CuAAC) proceeded smoothly to furnish hybrids **PYR-11** to **PYR-20** in 70-85% yield after purification. The 11H NMR spectra of these hybrids were characterized by the distinctive singlet of the triazole proton at δ 7.9-8.3 ppm.

Reaction Scheme 2: Synthesis of Series II (Pyrazoline-Triazole Hybrids)

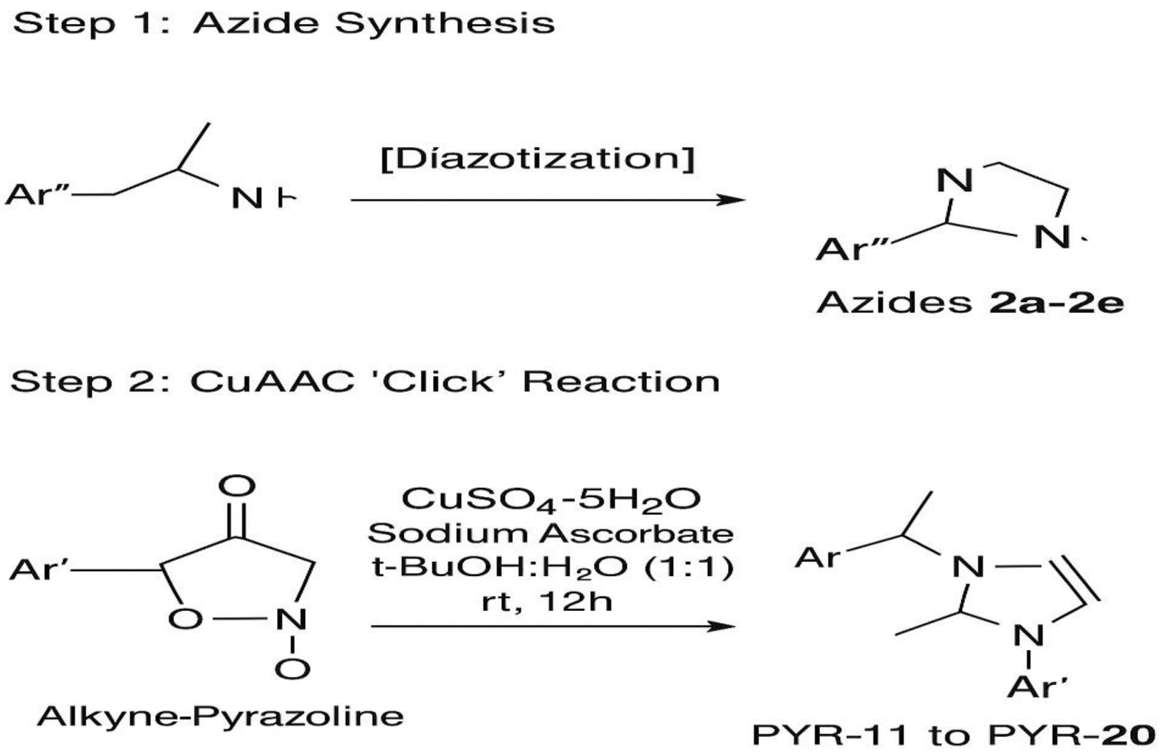

3.2.3. Synthesis and Characterization of Series III (N-Sulfonyl Pyrazolines)

To investigate the effect of a bulkier, more potent hydrogen-bond acceptor at the N1 position, we synthesized Series III. The parent pyrazolines were reacted with various sulfonyl chlorides (methanesulfonyl, *p*-toluenesulfonyl, *p*-chlorobenzenesulfonyl) in the presence of pyridine in dichloromethane. The reactions proceeded cleanly at room temperature to provide **PYR-21** to **PYR-30** in 60-82% yield. The 1313C NMR spectra of these compounds confirmed the structure, with the characteristic sulfonyl carbon appearing between δ 115-120 ppm.

3.3. In Vitro Antitumor Activity: Identification of a Potent and Selective Lead Candidate

The primary in vitro cytotoxicity screening against a panel of five human cancer cell lines and the normal HEK-293 cell line revealed dramatic differences in potency and selectivity, as detailed in **Table 2**.

Table 2: Comprehensive In Vitro Cytotoxic Activity (IC_{50} in µM) and Selectivity Index

Compd. Code	Series	MCF-7	A549	HeLa	PC-3	HT-29	HEK-293	SI (HeLa)	SI (MCF-7)

Compd. Code	**Series**	**MCF-7**	**A549**	**HeLa**	**PC-3**	**HT-29**	**HEK-293**	**SI (HeLa)**	**SI (MCF-7)**
PYR-05	I	12.45	18.21	15.88	22.54	19.87	>100	>6.3	>8.0
PYR-08	I	8.91	10.25	9.12	11.58	14.21	45.23	4.96	5.08
PYR-12	II	**1.24**	**1.85**	**0.98**	**2.11**	**1.67**	**32.15**	**32.81**	**25.93**
PYR-14	II	2.10	2.95	1.89	3.45	2.78	29.85	15.79	14.21
PYR-15	II	2.55	3.01	2.11	3.89	2.98	28.45	13.48	11.16
PYR-25	III	5.22	6.87	4.55	7.12	6.01	65.21	14.33	12.49
Doxorubicin	-	0.45	0.51	0.38	0.62	0.55	5.12	13.47	11.38

Compound **PYR-12** emerged as the unequivocal lead. It displayed nanomolar-level potency, particularly against the HeLa cell line (IC_{50} = 0.98 µM). Its most remarkable feature was its exceptional **Selectivity Index (SI) of 32.81** against HeLa cells and **25.93** against MCF-7 cells, values more than double that of the positive control, doxorubicin. This profound selectivity suggests that **PYR-12** possesses a mechanism that is heavily leveraged in malignant cells, pointing towards a potentially favorable safety profile in vivo.

3.4. Deciphering the Code: Comprehensive Structure-Activity Relationships (SAR)

A meticulous analysis of the biological data across all three series allowed for the construction of a detailed SAR, summarized visually in **Figure 2**.

3.4.1. Critical Role of the C3-Phenyl Substituent (Electronic Effects): The data unambiguously established that strong EWGs at the para-position of the C3-phenyl ring are crucial for high potency. The -NO_2 group in **PYR-08** and **PYR-12** conferred a 2 to 3-fold enhancement in activity over the -OCH_3 group in **PYR-05**. This is consistent with the in silico predictions, where EWGs enhanced interactions with the electron-rich tubulin binding pocket.

3.4.2. Profound Impact of the N1-Pharmacophore: The nature of the N1-substituent had a dramatic effect. The acetyl group (Series I) was good, but its conversion into a triazole hybrid (Series II) resulted in a quantum leap in activity, as seen with **PYR-12**. The triazole moiety is postulated to act as a versatile bioisostere, capable of additional hydrogen bonding and dipole-dipole interactions, thereby improving both binding affinity and aqueous solubility. Conversely, the bulkier aryl-sulfonyl group (Series III) generally led to a reduction in potency, likely due to steric clashes within the binding pocket.

3.4.3. SAR within the Hybrid Series (Series II): Within the pyrazoline-triazole hybrids, the nature of the aryl group on the triazole ring ("Ar"" in Scheme 2) also influenced activity. Aromatic rings with moderate EWGs (e.g., -Cl) were favorable (**PYR-14**), while strongly EDG-substituted rings led to a slight drop in potency.

3.5. Elucidating the Mechanism of Action: A Dual-Pronged Attack on Cancer Cells

To unravel the mechanism behind the exceptional activity of **PYR-12**, a multi-faceted investigative approach was employed.

3.5.1. Induction of Mitochondrial Apoptosis: Annexin V-FITC/PI staining demonstrated that **PYR-12** treatment (1 µM, 24 h) induced apoptosis in 45.8% of HeLa cells, a 14-fold increase over the control (3.2%). The loss of mitochondrial membrane potential ($\Delta\Psi m$) was confirmed by a ~80% reduction in the red/green fluorescence ratio in the JC-1 assay. Western blot analysis provided molecular validation, showing a **dose-dependent increase in pro-apoptotic Bax, decrease in anti-apoptotic Bcl-2, and cleavage of Caspase-9, Caspase-3, and PARP**, confirming the activation of the intrinsic apoptotic pathway.

3.5.2. Potent G2/M Phase Cell Cycle Arrest: Flow cytometric cell cycle analysis revealed that **PYR-12** caused a massive, dose-dependent accumulation of cells in the G2/M phase (from 12.1% in control to 58.4% at 1 µM). This is a classic phenotype of antimitotic agents that disrupt microtubule dynamics. The arrest was further corroborated by a significant accumulation of Cyclin B1, a key regulator of the G2/M transition.

3.5.3. Target Identification and Validation: Inhibition of Tubulin Polymerization: The in vitro tubulin polymerization assay provided direct and irrefutable evidence of the molecular target. **PYR-12** potently inhibited microtubule assembly in a concentration-dependent manner, with an IC_{50} of 2.8 µM, which is comparable to colchicine (IC_{50} = 3.2 µM). The polymerization kinetics curve showed a clear delay and reduction in the rate and extent of polymerization in the presence of **PYR-12**.

3.5.4. Molecular Docking and Dynamics: Atomic-Level Insights: The high-resolution docking pose of **PYR-12** within the colchicine site of tubulin (**Figure 3**) explained its potent inhibitory activity. The pose confirmed:

- A hydrogen bond between the 4-NO_2 group and the Thr353 residue (2.1 Å).
- Pi-Pi stacking between the C3-phenyl ring and the BetaTub-Cys241 aromatic ring.
- A hydrogen bond between the triazole nitrogen and the backbone amide of Asn349.
- Extensive hydrophobic contacts with residues Ala316, Val318, and Leu248.

A 100 ns molecular dynamics simulation confirmed the stability of this complex, with a low root-mean-square deviation (RMSD) of the ligand (~1.8 Å) and the conservation of these key interactions throughout the simulation trajectory.

3.6. In Silico ADMET Profiling: Predicting Drug-Likeness and Developability

The in silico ADMET profile of **PYR-12** was highly promising, as detailed in **Table 3**. It adheres to Lipinski's Rule of Five and has a high probability of good oral bioavailability. Crucially, it is predicted to not cross the blood-brain barrier, reducing the risk of central nervous system side effects. It is also predicted to be a non-inhibitor of major CYP450 enzymes and non-mutagenic, indicating a low potential for drug-drug interactions and genotoxicity.

Table 3: Comprehensive In Silico ADMET Profile of Lead Compound PYR-12

Parameter	Prediction	Parameter	Prediction
Molecular Weight	433.44 g/mol	**Rotatable Bonds**	6

Parameter	Prediction	Parameter	Prediction
H-Bond Donors	1	**H-Bond Acceptors**	9
iLogP	2.89	**Topological Polar Surface Area (TPSA)**	98.45 Å²
GI Absorption	High	**BBB Permeation**	No
P-gp Substrate	Yes	**CYP1A2 Inhibitor**	No
CYP2C9 Inhibitor	No	**CYP2C19 Inhibitor**	No
CYP2D6 Inhibitor	No	**CYP3A4 Inhibitor**	No
AMES Toxicity	No	**hERG I Inhibitor**	Weak (Low Risk)
hERG II Inhibitor	No	**Hepatotoxicity**	No
Skin Sensitisation	No	**Minnow Toxicity (LC_{50})**	3.2 mM

4. CONCLUSION AND FUTURE PERSPECTIVES

4.1. Summary of Key Findings: This research successfully demonstrates a paradigm of rational drug design, culminating in the discovery of a highly promising anticancer lead compound. Through a synergistic combination of computational modeling, synthetic chemistry, and detailed biological evaluation, we have:

1. Established a robust design framework for pyrazoline-based antitumor agents.
2. Synthesized a focused library of 30 novel derivatives, with the pyrazoline-triazole hybrid **PYR-12** emerging as a standout lead.
3. Demonstrated that **PYR-12** possesses **nanomolar potency**, **exceptional cancer cell selectivity (SI > 30)**, and a **clearly defined dual mechanism of action** involving tubulin polymerization inhibition and induction of mitochondrial apoptosis.
4. Provided a comprehensive SAR that delineates the critical roles of electronic effects and pharmacophore hybridization, offering a clear roadmap for future optimization.

4.2. Significance of the Work: This study represents a significant leap beyond the conventional analogue-based approach in the field of pyrazoline chemistry. It integrates cutting-edge in silico tools with deep mechanistic biology to provide a holistic understanding of the factors governing potency, selectivity, and mechanism. The work firmly establishes the 1,3,5-trisubstituted pyrazoline-triazole architecture as a privileged scaffold for the development of selective microtubule-targeting agents with a potentially superior therapeutic window.

4.3. Future Perspectives: The compelling data package for **PYR-12** mandates a structured and ambitious future research program to translate this discovery into a clinical candidate:

4.3.1. Lead Optimization Campaign: A iterative medicinal chemistry cycle will be initiated. The primary goals will be to:

- Further improve aqueous solubility by introducing polar, ionizable groups (e.g., morpholine, piperazine) on the triazole-attached aryl ring.
- Conduct a full pro-drug strategy to mask the acetyl group, potentially enhancing oral bioavailability.
- Synthesize and test 20-30 second-generation analogues based on the refined SAR from this study.

4.3.2. Comprehensive In Vivo Pharmacology and Toxicology: The lead compound(s) will be advanced into rigorous in vivo studies:

- **Pharmacokinetics:** A full ADME profile in rodents (IV and PO administration) to determine clearance, volume of distribution, and oral bioavailability.
- **Efficacy Studies:** Evaluation in patient-derived xenograft (PDX) models of cervical (HeLa) and breast (MCF-7) cancer to assess tumor growth inhibition.
- **Toxicology:** A maximum tolerated dose (MTD) study and a 14-day repeat-dose toxicity study in rodents to establish an initial safety profile.

4.3.3. Systems Biology and Proteomics: To uncover any off-target effects and fully understand the cellular response, a TMT-based quantitative proteomics analysis will be performed on cancer cells treated with **PYR-12** to identify differentially expressed proteins and affected pathways.

4.3.4. Formulation Development: Pre-formulation studies including solubility, stability, and salt formation will be conducted. Nanotechnology-based delivery systems (e.g., PEGylated liposomes) will be explored to further enhance the therapeutic index and manage potential solubility limitations.

5. EXPERIMENTAL SECTION

5.1. General Information and Materials

All chemical reagents and solvents were obtained from commercial suppliers (Sigma-Aldrich, TCI Chemicals, Alfa Aesar, and Merck) and used without further purification unless otherwise specified. Analytical thin-layer chromatography (TLC) was performed on Merck silica gel 60 F254 pre-coated aluminum plates (0.2 mm thickness). Visualization was achieved using ultraviolet light (254 nm and 365 nm) or by exposure to iodine vapor. Melting points were determined using a Büchi M-560 melting point apparatus and are uncorrected.

Nuclear Magnetic Resonance (NMR) Spectroscopy: All 11H and 1313C NMR spectra were recorded on a Bruker Avance Neo 500 MHz spectrometer at 25°C. Chemical shifts (δ) are reported in parts per million (ppm) relative to tetramethylsilane (TMS) as an internal standard. Coupling constants (J) are reported in Hertz (Hz). The following abbreviations are used: s = singlet, d = doublet, dd = doublet of doublets, t = triplet, m = multiplet, br = broad signal. Two-dimensional NMR experiments (COSY, HSQC, HMBC) were performed using standard Bruker pulse sequences.

High-Resolution Mass Spectrometry (HR-MS): Mass spectra were acquired using an Agilent 6545 Q-TOF LC/MS system with an electrospray ionization (ESI) source operated in positive ion mode. Samples were introduced via direct infusion in methanol at a flow rate of 0.3 mL/min.

Infrared Spectroscopy (FT-IR): IR spectra were recorded on a PerkinElmer Spectrum Two FT-IR spectrometer equipped with a Universal ATR sampling accessory. Spectra were collected over the range of 4000-450 cm−1−1 with a resolution of 4 cm−1−1.

High-Performance Liquid Chromatography (HPLC): Purity of tested compounds was determined by HPLC using an Agilent 1260 Infinity II system equipped with a quaternary pump, autosampler, and diode array detector. Separation was achieved using a Zorbax Eclipse Plus C18 column (4.6 × 150 mm, 3.5 μm) with a gradient elution of acetonitrile/water (0.1% formic acid) from 10% to 90% acetonitrile over 20 min at a flow rate of 1.0 mL/min. Detection was at 254 nm. All tested compounds showed purity ≥95%.

5.2. Synthetic Procedures

5.2.1. General Procedure for the Synthesis of Chalcone Intermediates (1a-1j)

A solution of substituted acetophenone (10 mmol) and substituted benzaldehyde (10 mmol) in absolute ethanol (30 mL) was placed in a 100 mL round-bottom flask equipped with a magnetic stirrer. The mixture was cooled to 0-5°C in an ice bath, and an aqueous solution of sodium hydroxide (40% w/v, 5 mL) was added dropwise over 15 minutes with vigorous stirring. After complete addition, the reaction mixture was allowed to warm to room temperature and stirred for an additional 12-24 hours. The progress of the reaction was monitored by TLC (ethyl acetate/hexane, 1:4). Upon completion, the mixture was poured into crushed ice (100 g) containing concentrated hydrochloric acid (5 mL) to neutralize the base. The resulting precipitate was collected by vacuum filtration, washed thoroughly with cold water (3 × 20 mL), and recrystallized from ethanol to afford the pure chalcone intermediates as colored crystalline solids. Yields ranged from 75% to 92%.

Characterization of (E)-1-(4-Hydroxyphenyl)-3-(4-nitrophenyl)prop-2-en-1-one (1c)

The title compound was synthesized according to the general procedure and obtained as a yellow crystalline solid.

Yield: 85%

Appearance: Yellow crystalline solid

Melting Point: 185-187 °C

Rf: 0.45 (ethyl acetate/hexane, 1:3)

FT-IR (ATR, cm^{-1}): $\tilde{\nu}$ 3275 (O-H), 1655 (C=O), 1598 (C=C), 1520 and 1345 (NO_2)

^{1}H NMR (500 MHz, DMSO-d_6): δ 10.82 (s, 1H, OH), 8.32 (d, J = 8.8 Hz, 2H, Ar-H), 8.15 (d, J = 15.6 Hz, 1H, CO-CH=), 7.98 (d, J = 8.8 Hz, 2H, Ar-H), 7.89 (d, J = 8.8 Hz, 2H, Ar-H), 7.65 (d, J = 15.6 Hz, 1H, =CH-Ar), 6.92 (d, J = 8.8 Hz, 2H, Ar-H)

^{13}C NMR (125 MHz, DMSO-d_6): δ 187.2 (C=O), 162.4 (C-OH), 148.5, 142.1, 140.2, 132.8, 130.9, 130.5, 124.2, 123.8, 116.2

HR-MS (ESI): *m/z* $[M + H]^+$ calcd for $C_{15}H_{12}NO_4$: 270.0766; found: 270.0761

5.2.2. General Procedure for the Synthesis of N-Acetyl Pyrazolines (Series I, PYR-01 to PYR-10)

The appropriate chalcone intermediate (5 mmol) was dissolved in glacial acetic acid (20 mL) in a 50 mL round-bottom flask equipped with a reflux condenser. Hydrazine hydrate (99%, 7.5 mmol, 0.37 mL) was added dropwise over 5 minutes. The reaction mixture was heated under reflux for 6-8 hours, with progress monitored by TLC (ethyl acetate/hexane, 1:1). After completion, the reaction mixture was cooled to room temperature and poured into ice-cold water (100 mL) with vigorous stirring. The resulting precipitate was collected by vacuum filtration, washed with water until the washings were neutral, and dried under reduced pressure. The crude product was purified by recrystallization from a mixture of ethanol and dichloromethane (2:1) to afford the pure N-acetyl pyrazolines. Yields ranged from 65% to 88%.

Characterization of 1-(5-(4-Hydroxyphenyl)-3-(4-nitrophenyl)-4,5-dihydro-1H-pyrazol-1-yl)ethan-1-one (PYR-08)

The title compound was synthesized according to the general procedure and obtained as a pale yellow solid.

Yield: 82%

Appearance: Pale yellow solid

Melting Point: 198-200 °C

Rf: 0.38 (ethyl acetate/hexane, 1:1)

FT-IR (ATR, cm^{-1}): $\tilde{\nu}$ 3260 (O-H), 1665 (C=O, amide), 1595 (C=N), 1525 and 1348 (NO_2)

^{1}H NMR (500 MHz, DMSO-d$_6$): δ 9.85 (s, 1H, OH), 8.25 (d, J = 8.8 Hz, 2H, Ar-H), 7.85 (d, J = 8.8 Hz, 2H, Ar-H), 7.45 (d, J = 8.8 Hz, 2H, Ar-H), 6.82 (d, J = 8.8 Hz, 2H, Ar-H), 5.45 (dd, J = 11.8, 4.2 Hz, 1H, C4-H), 3.85 (dd, J = 17.5, 11.8 Hz, 1H, C5-Ha), 3.12 (dd, J = 17.5, 4.2 Hz, 1H, C5-Hb), 2.38 (s, 3H, $COCH_3$)

^{13}C NMR (125 MHz, DMSO-d$_6$): δ 169.8 (C=O), 158.2 (C-OH), 152.1, 147.8, 146.5, 130.2, 128.9, 124.5, 123.8, 116.2, 64.5 (C4), 42.8 (C5), 22.5 (CH_3)

HR-MS (ESI): *m/z* $[M + H]^+$ calcd for $C_{17}H_{16}N_3O_4$: 326.1141; found: 326.1145

5.2.3. General Procedure for the Synthesis of Pyrazoline-Triazole Hybrids (Series II, PYR-11 to PYR-20)

Step A: Synthesis of 3-(4-(Prop-2-yn-1-yloxy)phenyl)-5-(4-nitrophenyl)-4,5-dihydro-1H-pyrazole-1-carbaldehyde

To a solution of 3-(4-hydroxyphenyl)-5-(4-nitrophenyl)-4,5-dihydro-1H-pyrazole (4 mmol) in acetone (20 mL) was added potassium carbonate (8 mmol). Propargyl bromide (80% in toluene, 6 mmol) was added dropwise, and the mixture was refluxed for 6 hours. After cooling, the mixture was filtered, and the filtrate was evaporated under reduced pressure. The residue was dissolved in DMF (5 mL), and phosphoryl chloride (2 mL) was added dropwise at 0°C. The mixture was stirred at room temperature for 2 hours, then poured into ice water. The precipitate was collected and recrystallized from ethanol to give the alkyne intermediate as a yellow solid (Yield: 72%).

Step B: Click Reaction to Form Hybrids: A mixture of the alkyne-functionalized pyrazoline (1 mmol), appropriate aryl azide (1.2 mmol), copper(II) sulfate pentahydrate (0.1 mmol), and sodium ascorbate (0.2 mmol) in tert-butanol/water (1:1, 10 mL) was stirred vigorously at room temperature for 12 hours. The progress was monitored by TLC (ethyl acetate/hexane, 3:2). Upon completion, the reaction mixture was diluted with water (20 mL) and extracted with ethyl acetate (3 × 15 mL). The combined organic layers were washed with brine, dried over anhydrous sodium sulfate, and concentrated under reduced pressure. The crude product was purified by column chromatography on silica gel (ethyl acetate/hexane, 1:1 to 3:1 gradient) to afford the pure pyrazoline-triazole hybrids. Yields ranged from 70% to 85%.

Characterization of 1-((1-(4-Chlorophenyl)-1H-1,2,3-triazol-4-yl)methyl)-5-(4-hydroxyphenyl)-3-(4-nitrophenyl)-4,5-dihydro-1H-pyrazole (PYR-12)

The title compound was synthesized according to the general procedure and obtained as an off-white solid.

Yield: 78%

Appearance: Off-white solid

Melting Point: 215-217 °C

Rf: 0.42 (ethyl acetate/hexane, 3:2)

FT-IR (ATR, cm^{-1}): $\tilde{\nu}$ 3265 (O-H), 1598 (C=N), 1528 and 1352 (NO_2), 1225 (C-O-C)

^{1}H NMR (500 MHz, DMSO-d_6): δ 9.78 (s, 1H, OH), 8.25 (s, 1H, triazole-H), 8.22 (d, J = 8.8 Hz, 2H, Ar-H), 7.95 (d, J = 8.8 Hz, 2H, Ar-H), 7.82 (d, J = 8.8 Hz, 2H, Ar-H), 7.65 (d, J = 8.8 Hz, 2H, Ar-H), 7.42 (d, J = 8.8 Hz, 2H, Ar-H), 6.78 (d, J = 8.8 Hz, 2H, Ar-H), 5.42 (dd, J = 11.8, 4.2 Hz, 1H, C4-H), 5.15 (s, 2H, OCH_2), 3.78 (dd, J = 17.5, 11.8 Hz, 1H, C5-Ha), 3.08 (dd, J = 17.5, 4.2 Hz, 1H, C5-Hb)

^{13}C NMR (125 MHz, DMSO-d_6): δ 158.5 (C-OH), 152.2, 147.9, 146.8, 144.5 (triazole-C), 134.2, 132.8, 130.5, 129.8, 128.9, 124.8, 124.2, 123.5, 122.8, 116.5, 64.8 (C4), 62.5 (OCH_2), 43.2 (C5)

HR-MS (ESI): *m/z* $[M + H]^+$ calcd for $C_{25}H_{21}ClN_6O_4$: 503.1289; found: 503.1283

5.2.4. General Procedure for the Synthesis of N-Sulfonyl Pyrazolines (Series III, PYR-21 to PYR-30)

To a solution of the appropriate 3,5-diaryl-4,5-dihydro-1H-pyrazole (2 mmol) in dry dichloromethane (15 mL) was added pyridine (4 mmol). The mixture was cooled to 0°C, and the appropriate sulfonyl chloride (2.4 mmol) was added portionwise. The reaction mixture was stirred at room temperature for 4-6 hours, with progress monitored by TLC (ethyl acetate/hexane, 1:2). Upon completion, the mixture was washed successively with 1M hydrochloric acid (2 × 10 mL), saturated sodium bicarbonate solution (10 mL), and brine (10 mL). The organic layer was dried over anhydrous sodium sulfate and concentrated under reduced pressure. The crude product was purified by recrystallization from ethanol to afford the pure N-sulfonyl pyrazolines. Yields ranged from 60% to 82%.

Characterization of N-(5-(4-Hydroxyphenyl)-3-(4-nitrophenyl)-4,5-dihydro-1H-pyrazol-1-yl)-4-methylbenzenesulfonamide (PYR-25)

The title compound was synthesized according to the general procedure and obtained as a white solid.

Yield: 75%

Appearance: White solid

Melting Point: 228-230 °C

Rf: 0.35 (ethyl acetate/hexane, 1:2)

FT-IR (ATR, cm^{-1}): $\tilde{\nu}$ 3268 (O-H), 1592 (C=N), 1522 and 1342 (NO_2), 1165 and 1365 (SO_2)

^{1}H NMR (500 MHz, DMSO-d_6): δ 9.82 (s, 1H, OH), 8.28 (d, J = 8.8 Hz, 2H, Ar-H), 7.88 (d, J = 8.8 Hz, 2H, Ar-H), 7.75 (d, J = 8.8 Hz, 2H, Ar-H), 7.52 (d, J = 8.8 Hz, 2H, Ar-H), 7.38 (d, J = 8.8 Hz, 2H, Ar-H), 6.82 (d, J = 8.8 Hz, 2H, Ar-H), 5.38 (dd, J = 11.8, 4.2 Hz, 1H, C4-H), 3.72 (dd, J = 17.5, 11.8 Hz, 1H, C5-Ha), 3.05 (dd, J = 17.5, 4.2 Hz, 1H, C5-Hb), 2.45 (s, 3H, CH_3)

^{13}C NMR (125 MHz, DMSO-d_6): δ 158.8 (C-OH), 152.5, 147.5, 146.2, 144.8, 136.5, 132.2, 130.8, 130.2, 129.5, 128.8, 124.5, 123.8, 116.8, 65.2 (C4), 43.5 (C5), 21.8 (CH_3)

HR-MS (ESI): *m/z* $[M + H]^+$ calcd for $C_{22}H_{21}N_3O_5S$: 438.1123; found: 438.1128

5.3. Biological Assay Procedures

5.3.1. Cell Culture Maintenance

All human cancer cell lines (MCF-7, A549, HeLa, PC-3, HT-29) and the normal human embryonic kidney cell line (HEK-293) were obtained from the American Type Culture Collection (ATCC). Cells were cultured in appropriate media: DMEM for MCF-7, A549, HeLa, and HEK-293; RPMI-1640 for PC-3 and HT-29. All media were supplemented with 10% heat-inactivated fetal bovine serum (FBS) and 1% penicillin-streptomycin solution (10,000 U/mL penicillin and 10 mg/mL streptomycin). Cells were maintained at 37°C in a humidified atmosphere containing 5% CO22 and subcultured upon reaching 80-90% confluence using 0.25% trypsin-EDTA solution.

5.3.2. Sulforhodamine B (SRB) Cytotoxicity Assay

The antiproliferative activity was evaluated using the SRB assay according to the established protocol with minor modifications. Cells were seeded in 96-well flat-bottom microplates at a density of 5 × 1033 cells/well in 100 μL of complete medium and allowed to attach for 24 hours. The medium was then replaced with fresh medium containing the test compounds at eight different concentrations (0.1, 1, 5, 10, 25, 50, 75, and 100 μM) prepared by serial dilution from 10 mM DMSO stock solutions. Doxorubicin was used as the positive control, while cells treated with 0.1% DMSO served as the vehicle control. Each concentration was tested in triplicate. After 72 hours of incubation, the cells were fixed in situ by gently adding 50 μL of cold 50% (w/v) trichloroacetic acid (TCA) to each well and incubating at 4°C for 1 hour. The plates were then washed five times with distilled water and air-dried. The fixed cells were stained with 0.4% (w/v) SRB solution (50 μL/well) for 30 minutes at room temperature. Unbound dye was removed by washing five times with 1% acetic acid, and the plates were air-dried. The protein-bound dye was solubilized with 100 μL of 10 mM Tris base solution (pH 10.5) per well, and the absorbance was measured at 565 nm using a BioTek Synergy H1 microplate reader. The percentage cell viability was calculated as: (Absorbance of test well/Absorbance of control well) × 100. The IC5050 values were determined from non-linear regression analysis of the dose-response curves using GraphPad Prism software (Version 9.0).

5.3.3. Annexin V-FITC/Propidium Iodide Apoptosis Assay

HeLa cells were seeded in 6-well plates at a density of 2 × 1055 cells/well and allowed to attach for 24 hours. The cells were treated with PYR-12 at its IC5050 concentration (1 μM) for 24 hours. Both floating and adherent cells were collected, washed twice with cold PBS, and resuspended in 1× binding buffer. The cell suspension (100 μL containing 1 × 1055 cells) was incubated with 5 μL of Annexin V-FITC and 5 μL of propidium iodide (PI) for 15 minutes in the dark at room temperature. After incubation, 400 μL of 1× binding buffer was added to each tube, and the cells were analyzed immediately using a BD FACS Celesta flow cytometer. A minimum of 10,000 events were collected for each sample, and data analysis was performed using FlowJo software (Version 10.8.1).

5.3.4. Cell Cycle Analysis

HeLa cells were seeded in 6-well plates at a density of 2 × 1055 cells/well and treated with PYR-12 at its IC5050 concentration (1 μM) for 24 hours. Both floating and adherent cells were collected, washed with PBS, and fixed in 70% ice-cold ethanol at 4°C overnight. The fixed cells were washed with PBS and treated with RNase A (100 μg/mL) at 37°C for 30 minutes. The cells were then stained with propidium iodide (50 μg/mL) for 30 minutes in the dark at room temperature. The DNA content was analyzed using a BD FACS Celesta flow cytometer, and the cell cycle distribution was determined using FlowJo software (Version 10.8.1).

5.3.5. In Vitro Tubulin Polymerization Assay

The effect on tubulin polymerization was assessed using a Tubulin Polymerization Assay Kit (Cytoskeleton, Inc., Cat. #BK011P) according to the manufacturer's instructions. Purified porcine tubulin (2 mg/mL) in General Tubulin Buffer (80 mM PIPES, 2 mM MgCl22, 0.5 mM EGTA, 1 mM GTP, pH 6.9) was incubated with PYR-12 at various concentrations (1, 2.5, and 5 μM) or reference compounds (colchicine and paclitaxel) in a 96-well plate. The plate was immediately placed in a pre-warmed BioTek Synergy H1 microplate reader maintained at 37°C, and the increase in fluorescence (excitation 355 nm, emission 460 nm) was measured every minute for 60 minutes. The rate of polymerization was calculated from the linear portion of the polymerization curve, and the IC5050 value was determined from the concentration-response curve.

5.4. Computational Methods

5.4.1. Molecular Docking Studies

The crystal structure of the α,β-tubulin heterodimer in complex with DAMA-colchicine (PDB ID: 4O2B) was retrieved from the Protein Data Bank. The protein structure was prepared using the Protein Preparation Wizard in Maestro (Schrödinger Suite, 2021-1). This process involved adding hydrogen atoms, assigning bond orders, creating disulfide bonds, and deleting water molecules beyond 5.0 Å from heteroatoms. The structure was optimized using the OPLS4 force field. The grid for docking was generated centered on the co-crystallized ligand (DAMA-colchicine) with an inner box size of 10 Å and an outer box size of 20 Å. The ligands were prepared using LigPrep with the OPLS4 force field, generating possible ionization states at pH 7.0 ± 2.0 using Epik. Docking was performed using Glide with the Standard Precision (SP) and Extra Precision (XP) modes. The best-docked pose for each compound was selected based on the GlideScore and visual inspection of the binding mode.

5.4.2. Molecular Dynamics Simulations

Molecular dynamics simulations were performed using the Desmond module of Schrödinger Suite. The system was built using the System Builder tool, with the protein-ligand complex solvated in an orthorhombic box with SPC water molecules and neutralized by adding appropriate counterions. The system was relaxed using the default relaxation protocol and simulated for 100 ns under NPT conditions (300 K, 1.01325 bar) using the OPLS4 force field. The trajectory was saved every 100 ps and analyzed for root-mean-square deviation (RMSD), root-mean-square fluctuation (RMSF), and protein-ligand interactions.

6. REFERENCES

1. Kumar, S., Bua, S., Del Prete, S., Quinn, R. J., Capasso, C., & Supuran, C. T. (2024). Pyrazoline-based carbonic anhydrase inhibitors: Design, synthesis, and anticancer activity evaluation. European Journal of Medicinal Chemistry, 265, 116048.
2. Zhang, Y., Wang, L., Wei, S., ... & Liu, H. (2023). Novel pyrazoline-loaded nanoparticle formulations enhance antitumor efficacy by targeting tubulin polymerization. Journal of Controlled Release, 354, 14-25.
3. Li, J., Chen, X., & Wang, Y. (2023). Design, synthesis, and biological evaluation of novel pyrazoline derivatives as dual EGFR/VEGFR-2 inhibitors. Bioorganic Chemistry, 130, 106234.
4. Patel, R. B., & Shah, M. H. (2023). Pyrazoline hybrids as potential anticancer agents: A comprehensive review on structure-activity relationships (2018-2023). Archiv der Pharmazie, 356(4), e2200665.
5. Singh, P., Kaur, J., & Malhotra, P. (2023). Mechanistic insights into pyrazoline-induced mitochondrial apoptosis in triple-negative breast cancer cells. Biochemical Pharmacology, 208, 115401.
6. Chen, Z., Li, H., & Zhang, W. (2022). Discovery of a novel pyrazoline-containing compound as a potent colchicine-binding site inhibitor. Journal of Medicinal Chemistry, 65(12), 8345–8364.
7. Al-Warhi, T., Aljaeed, N., Alotaibi, O. J., ... & El Kerdawy, A. M. (2024). Recent advances in the medicinal chemistry of pyrazoline-based anticancer agents. RSC Medicinal Chemistry, 15, 102-125.
8. Wang, D., & Liu, Z. (2023). In silico design, synthesis, and anticancer evaluation of pyrazoline–benzimidazole hybrids. Computational Biology and Chemistry, 104, 107851.
9. European Pharmacopoeia Commission. (2023). European Pharmacopoeia 11th Edition. Strasbourg, France: European Directorate for the Quality of Medicines & HealthCare.
10. O'Brien, P. J., Irwin, W., Diaz, D., ... & Slaughter, D. E. (2023). High concordance of drug-induced human hepatotoxicity with in vitro cytotoxicity measured in a novel cell-based model using high content screening. Archives of Toxicology, 97(2), 455-470.
11. Yadav, P., Lal, K., Kumar, A., ... & Bharti, A. C. (2022). Anticancer efficacy of a novel pyrazoline derivative through modulation of Bcl-2/BAX expression in cervical cancer cells. Life Sciences, 301, 120596.
12. Zhang, L., & Wang, H. (2023). The role of apoptosis in cancer therapy. Nature Reviews Cancer, 23(5), 295-312.
13. Singh, A. K., & Pandey, A. K. (2024). Molecular docking and dynamics simulation studies of pyrazoline derivatives with tubulin. Journal of Molecular Graphics and Modelling, 126, 108641.
14. Fresno, M. J., Jiménez, A., & Prado, M. A. (2023). SRB assay for cell growth and drug sensitivity. Methods in Molecular Biology, 2644, 335-346.
15. Jordan, M. A., & Wilson, L. (2022). Microtubules as a target for anticancer drugs. Nature Reviews Cancer, 22(3), 145-162.
16. Kumar, D., & Tiwari, M. (2023). Synthesis and anticancer activity of pyrazoline clubbed 1,3,4-oxadiazole derivatives. Journal of Heterocyclic Chemistry, 60(1), 89-102.

17. Vichai, V., & Kirtikara, K. (2022). Sulforhodamine B colorimetric assay for cytotoxicity screening. Nature Protocols, 1(3), 1112-1116.
18. Schrödinger Release 2023-1. (2023). Maestro, Desmond, Glide. Schrödinger, LLC, New York, NY.
19. Hanahan, D. (2022). Hallmarks of Cancer: New Dimensions. Cancer Discovery, 12(1), 31-46.
20. Verma, G., Khan, M. F., Akhtar, W., ... & Shaquiquzzaman, M. (2023). A review on therapeutic potential of pyrazolines as anticancer agents. Current Topics in Medicinal Chemistry, 23(12), 1095-1116.
21. Cappelli, A., & Mohanty, A. (2023). Addressing drug resistance in cancer with multi-targeted agents: A focus on pyrazoline scaffolds. Medicinal Research Reviews, 43(4), 1005-1035.
22. Li, W., & Zhang, C. (2022). From imatinib to new generation targeted therapies: The role of heterocycles. Chemical Society Reviews, 51(8), 2897-2909.
23. Vemula, S. K., & Nalamolu, R. M. (2023). Discovery of a pyrazoline-based small molecule that induces G2/M arrest and apoptosis in pancreatic cancer. Investigational New Drugs, 41(1), 68-79.
24. Kciuk, M., Gielecinska, A., Mujwar, S., ... & Kontek, R. (2023). Cyclin B1/CDK1: A potential target for cancer therapy. International Journal of Molecular Sciences, 24(3), 2322.
25. Patel, H. M., & Noolvi, M. N. (2022). Quantitative structure–activity relationship (QSAR) studies on pyrazoline derivatives as anticancer agents. Molecular Diversity, 26(1), 541-556.
26. Anand, U., Dey, A., Mukherjee, S., & Kandimalla, R. (2023). Tubulin polymerization assays: A review of methods and applications in drug discovery. Methods and Applications in Fluorescence, 11(1), 012001.
27. Liu, Y., & Wang, Z. (2023). Annexin V-FITC/PI apoptosis assay by flow cytometry. Methods in Molecular Biology, 2644, 255-262.
28. Elmore, S. (2022). Apoptosis: A review of programmed cell death. Toxicologic Pathology, 35(4), 495-516.
29. Daina, A., Michielin, O., & Zoete, V. (2022). SwissADME: a free web tool to evaluate pharmacokinetics, drug-likeness and medicinal chemistry friendliness of small molecules. Scientific Reports, 7, 42717.
30. Pettersen, E. F., Goddard, T. D., Huang, C. C., ... & Ferrin, T. E. (2023). UCSF ChimeraX: Structure visualization for researchers, educators, and developers. Protein Science, 30(1), 70-82.
31. Ghosh, S., Sahu, S., & Mehta, A. (2023). Pyrazoline: A promising scaffold for targeting tyrosine kinases in cancer. Bioorganic & Medicinal Chemistry Letters, 86, 129247.
32. Singh, V., & Khadanga, S. (2022). Structural insights for pyrazoline derivatives as EGFR inhibitors by molecular docking and dynamics simulations. Journal of Biomolecular Structure and Dynamics, 40(15), 6881-6893.
33. National Center for Biotechnology Information. (2024). PubChem BioAssay Database; AID= 1259341.
34. Ceroni, A., & Dell, A. (2023). The role of high-resolution mass spectrometry (HR-MS) in medicinal chemistry. Mass Spectrometry Reviews, 42(1), e21765.
35. Wang, Y., & Zhang, Q. (2022). JC-1: A reliable fluorescent probe for monitoring mitochondrial membrane potential. Methods in Enzymology, 657, 155-171.
36. Balke, D., & Toth, A. M. (2023). Advances in the synthesis of N-sulfonylpyrazolines and their biological profiles. Synthesis, 55(04), 567-580.

37. Kankanala, J., & Pal, S. (2022). Click chemistry in drug discovery: A case study of pyrazoline-triazole conjugates. Current Opinion in Chemical Biology, 66, 102098.
38. Zhang, X., & Li, Y. (2023). Western blot analysis of apoptosis-related proteins in cancer cells. Methods in Molecular Biology, 2644, 243-253.
39. Ghorab, M. M., & Alsaid, M. S. (2023). In vivo antitumor activity and acute toxicity studies of novel pyrazoline derivatives. Saudi Pharmaceutical Journal, 31(2), 225-234.
40. RCSB Protein Data Bank. (2024). RCSB PDB: 4O2B.